Astronomy & Astrophysics

GOODS-*Herschel*: dust attenuation properties of UV selected high redshift galaxies[⋆]

V. Buat[1], S. Noll[2], D. Burgarella[1], E. Giovannoli[1,3], V. Charmandaris[4,5,6], M. Pannella[7], H. S. Hwang[8], D. Elbaz[7], M. Dickinson[9], G. Magdis[10], N. Reddy[11], and E. J. Murphy[12]

[1] Aix-Marseille Université, CNRS – LAM (Laboratoire d'Astrophysique de Marseille) UMR 7326, 13388 Marseille, France
e-mail: veronique.buat@oamp.fr
[2] Institut für Astro- und Teilchenphysik, Universität Innsbruck, Technikerstr. 25/8, 6020 Innsbruck, Austria
[3] University of the Western Cape, Private Bag X17, 7535 Bellville, Cape Town, South Africa
[4] University of Crete, Department of Physics and Institute of Theoretical & Computational Physics, 71003 Heraklion, Greece
[5] IESL/Foundation for Research & Technology-Hellas, 71110 Heraklion, Greece
[6] Observatoire de Paris, LERMA (CNRS: UMR 8112), 61 Av. de l'Observatoire, 75014 Paris, France
[7] Laboratoire AIM-Paris-Saclay, CEA/DSM/Irfu – CNRS – Université Paris Diderot, CE-Saclay, 91191 Gif-sur-Yvette, France
[8] Smithsonian Astrophysical Observatory, 60 Garden St., Cambridge, MA 02138, USA
[9] National Optical Astronomy Observatory, 950 North Cherry Avenue, Tucson, AZ 85719, USA
[10] Department of Physics, University of Oxford, Keble Road, Oxford, OX1 3RH, UK
[11] Department of Physics and Astronomy, University of California, Riverside, 900 University Avenue, Riverside, 92521 California, USA
[12] *Spitzer* Science Center, California Institute of Technology, Pasadena, CA, 91125, USA

ABSTRACT

Context. Dust attenuation in galaxies is poorly known, especially at high redshift. And yet the amount of dust attenuation is a key parameter to deduce accurate star formation rates from ultraviolet (UV) rest-frame measurements. The wavelength dependence of the dust attenuation is also of fundamental importance to interpret the observed spectral energy distributions (SEDs) and to derive photometric redshifts or physical properties of galaxies.
Aims. We want to study dust attenuation at UV wavelengths at high redshift, where the UV is redshifted to the observed visible light wavelength range. In particular, we search for a UV bump and related implications for dust attenuation determinations.
Methods. We use photometric data in the *Chandra* Deep Field South (CDFS), obtained in intermediate and broad band filters by the MUSYC project, to sample the UV rest-frame of 751 galaxies with $0.95 < z < 2.2$. When available, infrared (IR) *Herschel*/PACS[⋆⋆] data from the GOODS-*Herschel* project, coupled with *Spitzer*/MIPS measurements, are used to estimate the dust emission and to constrain dust attenuation. The SED of each source is fit using the CIGALE code. The amount of dust attenuation and the characteristics of the dust attenuation curve are obtained as outputs of the SED fitting process, together with other physical parameters linked to the star formation history.
Results. The global amount of dust attenuation at UV wavelengths is found to increase with stellar mass and to decrease as UV luminosity increases. A UV bump at 2175 Å is securely detected in 20% of the galaxies, and the mean amplitude of the bump for the sample is similar to that observed in the extinction curve of the LMC supershell region. This amplitude is found to be lower in galaxies with very high specific star formation rates, and 90% of the galaxies exhibiting a secure bump are at $z < 1.5$. The attenuation curve is confirmed to be steeper than that of local starburst galaxies for 20% of the galaxies. The large dispersion found for these two parameters describing the attenuation law is likely to reflect a wide diversity of attenuation laws among galaxies. The relations between dust attenuation, IR-to-UV flux ratio, and the slope of the UV continuum are derived for the mean attenuation curve found for our sample. Deviations from the average trends are found to correlate with the age of the young stellar population and the shape of the attenuation curve.

Key words. galaxies: high-redshift – galaxies: ISM – galaxies: starburst – ultraviolet: galaxies – dust, extinction

1. Introduction

Although dust is a minor component in galaxies by mass, its effect on the observation of their stellar populations is striking. Dust captures a large fraction of the stellar emission, especially at short wavelengths. This process makes the direct observation of stellar populations from the UV to the near-IR, where they emit their light, insufficient to recover all the emitted photons. Reliable dust corrections are mandatory for measuring the star formation rate in the universe and its evolution with redshift

---

[⋆] Table of multi-colour photometry for the 751 galaxies is only available at the CDS via anonymous ftp to cdsarc.u-strasbg.fr (130.79.128.5) or via http://cdsarc.u-strasbg.fr/viz-bin/qcat?J/A+A/545/A141

[⋆⋆] *Herschel* is an ESA space observatory with science instruments provided by European-led Principal Investigator consortia and with important participation from NASA.

from UV-optical surveys. When dust emission is measured, accurate star formation rates can be derived by combining IR and UV data, but these data are often not available, in particular for deep optical surveys (e.g., Ilbert et al. 2010). As a consequence, it is particularly important to study the dependence of dust attenuation on parameters such as the observed luminosity, the stellar mass, or the slope of the UV continuum, since it could be used to correct large samples for the effect of dust attenuation, at least in a statistical way.

Any modelling of stellar populations in galaxies must also include attenuation from interstellar dust. Solving the radiation transfer in model galaxies is the best way to build physical and self-consistent SEDs. These models calculate the effective obscuration and produce attenuation curves as outputs, which are generally very different from the extinction curves affecting the flux of each star (e.g., Witt & Gordon 2000; Pierini et al. 2004; Tuffs et al. 2004; Panuzzo et al. 2007). However, these sophisticated models rely on numerous free parameters and physical assumptions that are difficult to constrain from the integrated emission from entire galaxies and for very large numbers of objects. Simpler models have been specifically developed to analyse large samples of galaxies, introducing attenuation curves, recipes, and/or templates. The number of free parameters is relatively small. These codes are often developed to measure photometric redshifts and physical parameters such as the star formation rate (SFR) and the stellar mass ($M_{\rm star}$). With the availability of mid and far-IR data for large samples of galaxies, new codes are emerging that combine stellar and dust emission on the basis of the balance between the stellar luminosity absorbed by dust and the corresponding luminosity re-emitted in the IR (da Cunha et al. 2008; Noll et al. 2009b).

Attenuation laws are introduced in all these codes, except for those which include a full radiation transfer treatment. The most popular attenuation curve is that of Calzetti et al. (2000), built for local starburst galaxies. Some specific recipes such as a time dependence of dust attenuation are sometimes introduced (Charlot & Fall 2000; Panuzzo et al. 2007).

The attenuation law for local starbursts, based on spectroscopic data, does not exhibit a bump at 2175 Å such as that observed in the extinction curves of the Milky Way (MW) or the Large Magellanic Cloud (LMC; Fitzpatrick & Massa 2007; Gordon et al. 2003). The presence of a UV bump in the attenuation curve of galaxies remains an open issue. In the nearby universe, the UV wavelength range has been investigated thanks to GALEX observations, but the results remain controversial. Wijesinghe et al. (2011) analyse the consistency of SFR indicators based on GALEX measurements in the far-ultraviolet (FUV) and near-ultraviolet (NUV) bands and fluxes in the H_{α} line, and conclude that they must consider an obscuration curve without any 2175 Å feature. Instead, from a careful analysis of pairs of galaxy SEDs, Wild et al. (2011) conclude that the UV slope of the attenuation curve is consistent with the presence of a bump at 2175 Å, a conclusion also reached by Conroy et al. (2010) from an analysis of the GALEX-SDSS colours of galaxies. At higher redshifts, several authors introduce a bump with moderate amplitude to improve photometric redshifts (Ilbert et al. 2009; Kriek et al. 2011). Direct evidence of bumps comes from the analysis of the galaxy spectra at $1 < z < 2.5$: Noll and collaborators analyse high quality spectra of ~200 galaxies and find significant bumps in at least 30% of the sources (Noll & Pierini 2005; Noll et al. 2007, 2009a). In an earlier paper, we analysed SEDs of 30 galaxies in a redshift range between 0.95 and 2.2, observed through intermediate band filters and with IR detections

from *Herschel*/PACS, and found evidence for a UV bump in the dust attenuation curve of all these galaxies (Buat et al. 2011b, hereafter Paper I). Selecting high-redshift galaxies on their observed optical colours is quite common (e.g. Lyman break or BzK galaxies, Reddy et al. 2008; Daddi et al. 2005, but most of the time mid- and far-IR data are not available for individual targets, making it difficult to obtain any direct measure of dust attenuation. Studies of dust emission often rely on stacking analyses, Rigopoulou et al. 2011; Burgarella et al. 2011; Reddy et al. 2012). The sensitivity of *Herschel* in the deepest fields allows us to combine stellar and dust emission for individual galaxies at high redshift (Wuyts et al. 2011), and to perform SED fitting accounting for both components (Paper I).

In this work, we will select galaxies at optical wavelengths with a very good sampling of their UV rest-frame SED: essentially, the sample is UV selected with a redshift range between 1 and 2. When available, IR emission from *Herschel*/PACS will be added to better constrain dust attenuation. SED fitting will be performed to estimate the main characteristics of dust attenuation. The sample and the SED fitting process are described in Sects. 2 and 3, respectively. The global amount of dust attenuation and its variation with stellar mass and UV luminosity are discussed in Sect. 4. Section 5 is devoted to the description of the attenuation law. In Sect. 6, we revisit the relation between dust attenuation and the slope of the UV continuum. Our conclusions are presented in Sect. 7. All magnitudes are given in the AB system. We assume that $\Omega_{\rm m} = 0.3$, $\Omega_{\Lambda} = 0.7$, and $H_0 = 70\,{\rm km\,s^{-1}\,Mpc^{-1}}$.

2. Galaxy sample and rest-frame UV continuum

2.1. Multi-wavelength data

As part of the GOODS-*Herschel* key programme (Elbaz et al. 2011), the *Herschel* Space Observatory (Pilbratt et al. 2010) surveyed part of the Great Observatories Origins Deep Survey Southern field (GOODS-S): $10' \times 10'$ centred on the CDFS were observed at 100 and 160 μm over 264 h by the PACS instrument (Poglitsch et al. 2010). These are the deepest images of the universe ever obtained with PACS.

Cardamone et al. (2010, the MUSYC project) compiled a uniform catalogue of optical and IR photometry for sources in GOODS-S, incorporating the GOODS *Spitzer* IRAC and MIPS data (Dickinson et al. 2003) and optical WFI broad-band data obtained at the ESO MPG 2.2 m telescope (Hildebrandt et al. 2006). In addition, they used deep intermediate-band imaging from the Subaru telescope to provide photometry with finer wavelength sampling than is possible from standard broad-band data. This was done to enable more accurate photometric redshifts, and it provides a valuable means of tracing the detailed shape of the UV rest-frame spectrum. The GOODS-S field defined for the MUSYC project is larger than that observed by *Herschel*. In order to be able to put constraints on the emission of the sources in the far-IR, we restrict the field to that observed by the GOODS-*Herschel* programme.

In Paper I, we selected 30 galaxies that are strongly detected from the UV to the far-IR, and whose rest-frame UV was sampled by several intermediate-band filters. In the present work, we select a much larger sample of galaxies by relaxing the constraint on the wavelength coverage and keeping galaxies without IR data. We start with the MUSYC catalogue, selecting sources with a spectroscopic redshift between 0.95 and 2.2. In this redshift range we have more than ten photometric bands available in the UV rest-frame and a good sampling around 2175 Å. As
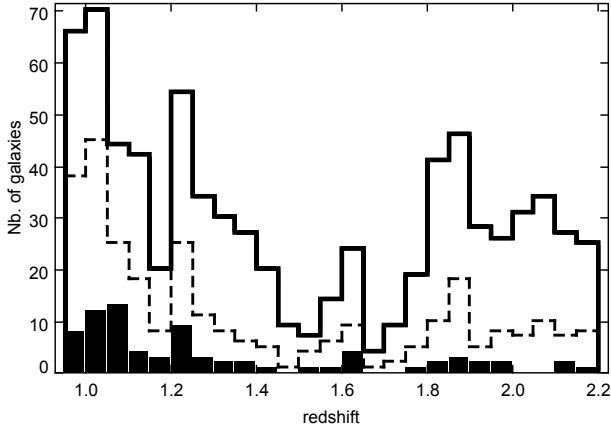
Fig. 1. Redshift distribution of the galaxy sample. The distribution for the whole sample is plotted as a solid line, that for the galaxies detected by MIPS with a dashed line, and the filled histogram corresponds to the redshifts of sources detected with PACS.

in Paper I, we consider all the optical broad bands (U, $U38$, B, V, R, I, z) and intermediate-band filters whose 5σ depth was fainter than 25 ABmag ($IA - 427$, 445, 484, 505, 527, 550, 574, 598, 624, 651, 679, and 738 (Cardamone et al. 2010, Table 2; Paper I, Fig. 1). We apply the same selection criteria as in Paper I to ensure that sources have data below rest-frame 1800 Å: a 5σ detection in the U and $U38$ filters for sources at $z < 1.6$, and in the B band and one intermediate filter corresponding to $\lambda < 1800$ Å in the galaxy rest-frame for $z > 1.6$. We further restrict the sample to galaxies without a X-ray detection according to Cardamone et al. (2008) to minimise the contribution of an AGN to either the IR or UV emission of the sources. Our sample contains 751 sources, all detected by IRAC at $3.6\,\mu$m. 726, 398, and 353 sources are detected at 4.5, 5.8, and 8 μm, respectively.

We cross-correlate these 751 sources with the GOODS-*Herschel* catalogue obtained from source extraction on the PACS images performed at the prior position of *Spitzer* 24 μm sources, as described in Elbaz et al. (2011). IRAC coordinates are used for the *Spitzer* 24 μm sources, and we adopt a tolerance radius between IRAC and optical coordinates equal to 1 arcsec. 290 sources have a 3σ detection at 24 μm. We check that all these sources have a single MIPS counterpart within a radius of 3 arcsec. 76 sources are detected at both 24 μm and 100 μm, and 30 at 24 μm, 100 μm, and 160 μm.

During our analysis, we will distinguish between galaxies that do and do not have detections of dust emission at 24 μm (hereafter MIPS data) and 100 μm (hereafter PACS data). Given the small number of sources with 160 μm detections, we will not isolate the galaxies also detected at this wavelength from those detected at 100 μm.

The redshift distribution of the sources is shown in Fig. 1. The bimodality comes from the original distribution of spectroscopic redshifts collected by Cardamone et al. (2010) and mainly reflects the difficulty to measure spectroscopic redshifts for galaxies at $1.4 < z < 1.8$. 55% of the galaxies selected have a redshift $z < 1.5$, and that percentage increases to 66 and 76% for the galaxies detected by MIPS and PACS respectively.

2.2. UV continuum

The UV continuum of star-forming galaxies is commonly modelled by a power-law, $f_\lambda(\text{erg cm}^{-2}\,\text{s}^{-1}\,\text{Å}^{-1}) \propto \lambda^\beta$, where β is called the slope of the UV continuum. The observational

determination of β is made either from spectra or from broad-band photometry, sometimes with large uncertainties depending on the broad-band filters considered (Buat et al. 2011b). The wavelength range over which β is measured also varies substantially (Calzetti 2001). Because of the very good sampling of the UV rest-frame continuum of our sources, we can accurately measure the slope of the UV continuum from 1300 to 3000 Å by performing a linear regression. The original wavelength range adopted by Calzetti et al. (1994) for fitting the UV continuum slope is $1200-2600$ Å. Meurer et al. (1999) adopted a narrower range, $1200-1800$ Å. However, given our available photometric data, extending the range to 3000 Å adds extra photometric points, which enable us to better constrain the UV continuum slope without significantly biasing the results that would be obtained from a shorter wavelength range. We start at 1300 Å to avoid the flattening of the UV continuum at shorter wavelengths, down to 1200 Å (Leitherer et al. 2002; Buat et al. 2002). β is calculated in two ways, with and without data corresponding to the wavelength of the UV bump, and both estimates are found to be very similar. This is due to the fact that we have a large number of photometric data for each source with only a few measures inside the bump area. In the following, we will use the values of β obtained with the full data set from 1300 to 3000 Å. The standard error on β is typically found to be of the order of 0.2. The rest-frame luminosity at 1530 Å of each galaxy is obtained by interpolation, using the result of the linear regression and the spectroscopic redshift of the source. In the following, we will define L_{FUV} as νL_ν at 1530 Å.

3. SED fitting with CIGALE

3.1. The CIGALE code

SED fitting is performed with the CIGALE code (Code Investigating GALaxy Emission)[1] developed by Noll et al. (2009b). This is a physically-motivated code that derives properties of galaxies by fitting their UV-to-IR SEDs. CIGALE combines a UV-optical stellar SED with a dust component emitting in the IR and fully conserves the energy balance between the dust absorbed stellar emission and its re-emission in the IR. We refer to Giovannoli et al. (2011) for details on the use of CIGALE to fit SEDs of actively star-forming distant galaxies observed in their rest-frame UV and IR. In the present work, the sampling of the UV range is very good, so we expect to constrain the dust attenuation curve. To model the attenuation by dust, the code uses as a baseline the attenuation law of Calzetti et al. (2000), and offers the possibility of varying the steepness of this law and adding a bump centred at 2175 Å. We refer to Noll et al. (2009b) for a complete description of the dust attenuation prescription. In brief, the dust attenuation is described as

$$A(\lambda) = \frac{A_V}{4.05}\left(k'(\lambda) + D_{\lambda_0,\gamma,E_b}(\lambda)\right)\left(\frac{\lambda}{\lambda_V}\right)^\delta, \quad (1)$$

where $\lambda_V = 5500$ Å, $k'(\lambda)$ comes from Calzetti et al. (2000) (Eq. (4)) and $D_{\lambda_0,\gamma,E_b}(\lambda)$, the Lorentzian-like Drude profile commonly used to describe the UV bump (Fitzpatrick & Massa 1990; Noll et al. 2009a), is defined as

$$D_{\lambda_0,\gamma,E_b} = \frac{E_b\lambda^2\gamma^2}{(\lambda^2 - \lambda_0^2)^2 + \lambda^2\gamma^2}. \quad (2)$$

---

[1] http://cigale.oamp.fr

Table 1. Input parameters for SED fitting with CIGALE.

Parameter	Symbol	Range
Dust component		
Distribution of dust mass	α	1, 1.5, 2, 2.5[1]
Amplitude of the bump	E_b	0, 0.5, 1, 1.5, 2.0, 2.5, 3, 3.5
Full width half maximum of the bump profile	γ	300, 350 Å[2]
Steepness of the attenuation law	δ	–0.8, –0.6, –0.4, –0.2, 0, 0.2
A_V for the young stellar population	$A_V(\text{ySP})$	0.25, 0.5, 0.75, 0.9, 1.05, 1.2, 1.35, 1.5, 1.65, 1.8 mag
Reduction of A_V for the old population	f_{att}	0.25, 0.5, 1[3]
Stellar component		
Age of the old stellar population	t_1	1, 2, 3, 4, 5 Gyr[4]
e-folding rate of the old stellar population	τ_1	1, 3 Gyr
Age of the young stellar population	t_2	0.01, 0.03, 0.1, 0.3 Gyr
Stellar mass fraction due to the young stellar population	f_{ySP}	0.01, 0.02, 0.05, 0.1, 0.2, 0.5

Notes. Values of input parameters defining the dust emission and attenuation recipes (first part of the table) and the stellar populations (second part of the table). [1] A single value of α ($\alpha = 2$) is used when PACS data are not available. [2] A single value of γ is used for each run of the code. The baseline value is 350 Å. [3] A single value of f_{att} is assumed for each run of the code. The baseline value is 0.5. [4] The age of the old stellar population is always lower than that of the universe at the redshift of the object.

The factor $\left(\frac{\lambda}{\lambda_V}\right)^\delta$ produces different slopes without modifying the visual attenuation A_V. It implies changes in the value of the effective total obscuration R_V, originally equal to 4.05 for the Calzetti et al. law (Noll et al. 2009b; Buat et al. 2011b).

The peak amplitude above the continuum, full width at half maximum, and central wavelength of the bump (E_b, γ, and λ_0) are free parameters of the code[2]. We fix the central wavelength of the bump λ_0 at 2175 Å. The full width at half maximum of the feature γ is not constrained by the SED fitting process. We adopt a value of 350 Å intermediate between the value found for the MW and LMC and that found by Noll et al. (2009a) for high-redshift systems. We also ran CIGALE with $\gamma = 300$ Å and checked that the exact value of this parameter has no influence on the determination of the other parameters. The input values for the other parameters are listed in Table 1. The range of values for each free parameter was chosen after many trials: we began with a very large range of values and then reduced the range by excluding values never chosen during the χ^2 minimisation. We will re-discuss the choice of the dust attenuation parameters in Sects. 4 and 5.

We adopt the stellar populations synthesis models of Maraston (2005). We consider a stellar population experiencing an exponentially decreasing star formation, whose age and e-folding time are free parameters. A younger stellar population with a constant SFR is added to the primary population. We adopt a Kroupa (2001) initial mass function (IMF). The two stellar components are linked by their mass fraction f_{ySP} and an attenuation correction is applied to each of them. The same attenuation law is assumed for both stellar populations and a reduction factor of the visual attenuation (expressed in magnitude), f_{att}, is applied to the old stellar population to account for the distributions of stars of different ages (Charlot & Fall 2000; Panuzzo et al. 2007). For our baseline model, f_{att} is fixed to 0.5, but we also performed runs with other values to check the validity of this assumption, since this parameter is ill-constrained (cf. Sect. 4).

Dust luminosities (L_{IR} between 8 and 1000 μm) are computed by fitting Dale & Helou (2002) templates and are linked to the attenuated stellar population models (the stellar luminosity absorbed by the dust is re-emitted in the IR). The validity of

Dale & Helou (2002) templates for measuring total IR luminosities of sources detected by *Herschel* is confirmed by the studies of Elbaz et al. (2010, 2011). When PACS data are not available, as is the case for the majority of the sources, only one of the templates of Dale & Helou (2002) is used, which corresponds to the exponent of the distribution of dust mass over heating intensity, α, equal to 2. This is the mean value of α obtained for the subsample of galaxies with PACS detection. This template is very close to that used by Wuyts et al. (2008). Using $\alpha = 2$ to extrapolate the predicted fluxes in the PACS bands gives values consistent with the PACS flux limits from Elbaz et al. (2011) for 88% of the sample at 100 μm (flux limit: 0.8 mJy) and the percentage increases to 92% at 160 μm (flux limit: 2.4 mJy). Adopting different values of α modifies these percentages. With $\alpha = 2.5$ corresponding to more quiescent and colder galaxies, only 6% of the predicted fluxes for galaxies not detected with PACS are found above the flux limits at 100 and 160 μm. For a hotter dust emission with $\alpha = 1.75$, the fraction of galaxies which would have been detected by PACS reaches 18% at 100 μm and 10% at 160 μm. Therefore we do not favour low values of α for the galaxies not detected in IR.

We run CIGALE on the full sample of 751 galaxies. The input parameters as well as additional output parameters like the stellar mass, the instantaneous SFR, or the total IR luminosity are estimated from the probability distribution function (PDF). The expectation value and its standard deviation are derived for each parameter. 84% of the sample is fitted with a minimum value of the reduced χ^2 lower than 3. The list of free parameters is given in Table 1.

Although we discarded sources with an X-ray detection (Sect. 2.1), highly obscured AGN could be present in our galaxy sample. To check this issue, we use the $F(24)/F(R)$ flux ratio: highly obscured Compton thick AGN are expected to exhibit $F(24)/F(R)$ flux ratios larger than few hundreds (Fiore et al. 2009). We also run CIGALE adding an AGN contribution as in Paper I (with two obscured AGN templates from the Siebenmorgen et al. (2004) library). In Fig. 2, we present the fraction of L_{IR} attributed to an obscured AGN by CIGALE as a function of $F(24)/F(R)$. The highest value of $F(24)/F(R)$ is 340. If we focus on galaxies with $F(24)/F(R) > 200$, only one source is found with an AGN fraction larger than 0.15. We discard this source from the following analysis. For the remaining sources, the average AGN fraction found by CIGALE is 0.09±0.07. Since

---

[2] E_b and γ are related to the original parameters c_3 and γ_{FM} introduced by Fitzpatrick & Massa (1990): $E_b = c_3/\gamma_{FM}^2$ and $\gamma = \gamma_{FM} \times \lambda_0^2$.
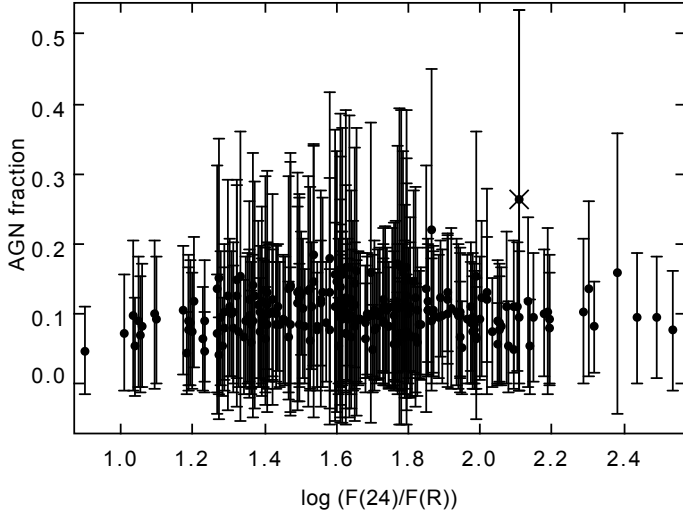
Fig. 2. Fraction of L_{IR} attributed to an obscured AGN by CIGALE as a function of the flux ratio at $24\,\mu$m and in the R band, the error bars represent the standard deviation calculated by CIGALE for this parameter. The cross indicates the only object with $F(24)/F(R) > 200$ and an AGN fraction higher than 0.15.

this low value is consistent with no AGN contribution, we will use the results of the SED fitting process without any AGN template in the following analysis.

3.2. Analysis of a catalogue of artificial galaxies

In order to check the robustness and accuracy of the parameter estimation, we generate a catalogue of artificial SEDs from the input catalogue. First, we run the code on the full dataset to select the best model for each galaxy that corresponds to a single SED. The catalogue of artificial sources is built by integrating the best SED of each galaxy in the observed bands. A random error, typically of the order of 10%, is added to the obtained fluxes. At the end, we have a sample of artificial galaxies whose properties and SEDs are expected to be representative of the real sources. The code is run on this artificial catalogue to compare the exact values of the physical parameters corresponding to the artificial SEDs to the parameters estimated by the code. With this catalogue, we want to check our ability to estimate individual output parameters of the code given the wavelength coverage. We do not attempt to measure the effects of different signal-to-noise ratios.

The results are summarised in Fig. 3 and Table 2. The sources detected with MIPS, with PACS and MIPS, and without any IR data are considered separately. For each parameter of interest in the present work, the correlation between the true and estimated values is shown in Fig. 3. The correlation coefficient between both quantities is reported in Table 2 along with the typical uncertainty. All parameters are better estimated when IR data are included. No clear difference is found when PACS data are used in addition to MIPS data to estimate L_{IR}: this is due to the way we choose the IR fluxes of the artificial galaxies. Indeed, the determination of L_{IR} for artificial sources with MIPS data does not account for a variation of the IR templates, since artificial galaxies are built with only one IR SED ($\alpha = 2$), also used to fit them. Therefore, L_{IR} is well constrained with only one value. The SFR and A_{FUV} strongly depend on the determination of L_{IR} and are also well determined with only one IR (MIPS) data point. Without IR data, L_{IR} appears to be

slightly overestimated, and as a consequence so are the SFR and A_{FUV}. We will re-discuss the determination of L_{IR} in the next subsection. The input parameters related to the star formation history are not well constrained: previous studies have also confirmed the weak constraints placed on these parameters (Noll et al. 2009b; Giovannoli et al. 2011; Buat et al. 2011a). The parameters describing the dust attenuation curve, E_b and δ, appear better constrained when IR data are available. The dynamical range of the estimated values is always lower than that of the true ones: the parameters are estimated as the mean of the PDF, which gives low weight to extreme values. In Sect. 5, we will re-discuss this effect, which strongly affects the determination of E_b.

3.3. SED fitting with and without IR data

It is important to check the robustness of the estimation of the most important parameters of this study against the availability of IR data. In complement to the analysis performed on artificial galaxies, we can also use the original sample with IR (MIPS or PACS data) to fit it with and without IR data and compare the estimated values of these parameters. We consider the sources detected by MIPS (290 galaxies) adding PACS data when available (for 76 galaxies). We run CIGALE on the SEDs of these galaxies without any IR data. In this case, only one IR SED is used with $\alpha = 2$ and L_{IR} is constrained by the obscuration of the UV-optical light. In Fig. 4, we compare the estimates of A_{FUV}, L_{IR}, E_b, and δ with and without considering IR data. The agreement between the estimates of all parameters is very good with correlation coefficients equal to 0.95 for A_{FUV}, L_{IR}, and E_b, and 0.92 for δ. The SED fitting without IR data is found to slightly overestimate dust attenuation and IR luminosities for small values of these parameters, by 0.27 mag for $A_{FUV} = 1$ mag and by 0.15 dex for $\log(L_{IR}) = 10.5$ [$L_\odot$]. It is qualitatively consistent with the analysis performed on artificial galaxies with an overestimate of 0.4 mag for $A_{FUV} = 1$ mag and 0.20 dex for $\log(L_{IR}) = 10.5$ [$L_\odot$] for artificial galaxies without IR data (Fig. 3). The discrepancy between exact and estimated values of A_{FUV} and L_{IR} is larger for artificial galaxies without IR data, with a slope between the true and estimated values of A_{FUV} and L_{IR} significantly different from 1 (see Fig. 3), than between these quantities estimated on real galaxies observed in IR and analysed with or without IR data (see Fig. 4). Most of the pseudo-galaxies without any IR data are intrinsically faint when compared to the galaxies detected in IR and plotted in Fig. 4. This difference together with the nature of the data (observed and artificial fluxes) can explain the relative discrepancies found in the two analyses performed here and in Sect. 3.2. The determination of E_b is found to be robust against the inclusion or neglection of IR data, whereas δ is more uncertain without IR data and is overestimated for low values of the parameter (by 0.1 units for $\delta = -0.5$). The latter result was also obtained with the catalogue of artificial galaxies.

3.4. Star formation history

As shown in Sect. 3.2, the detailed star formation history is not well constrained. The old stellar population is always found older than 1 Gyr, from $\simeq$1.5 Gyr at $z \simeq 2$ to $\simeq$3 Gyr at $z \simeq 1$. The average mass fraction locked in the young stars (f_{ySP}) is found to be of the order of 10%, which corresponds to galaxies with active star formation. In this work, we focus on the analysis of the UV part of the spectrum, which is dominated by the emission of
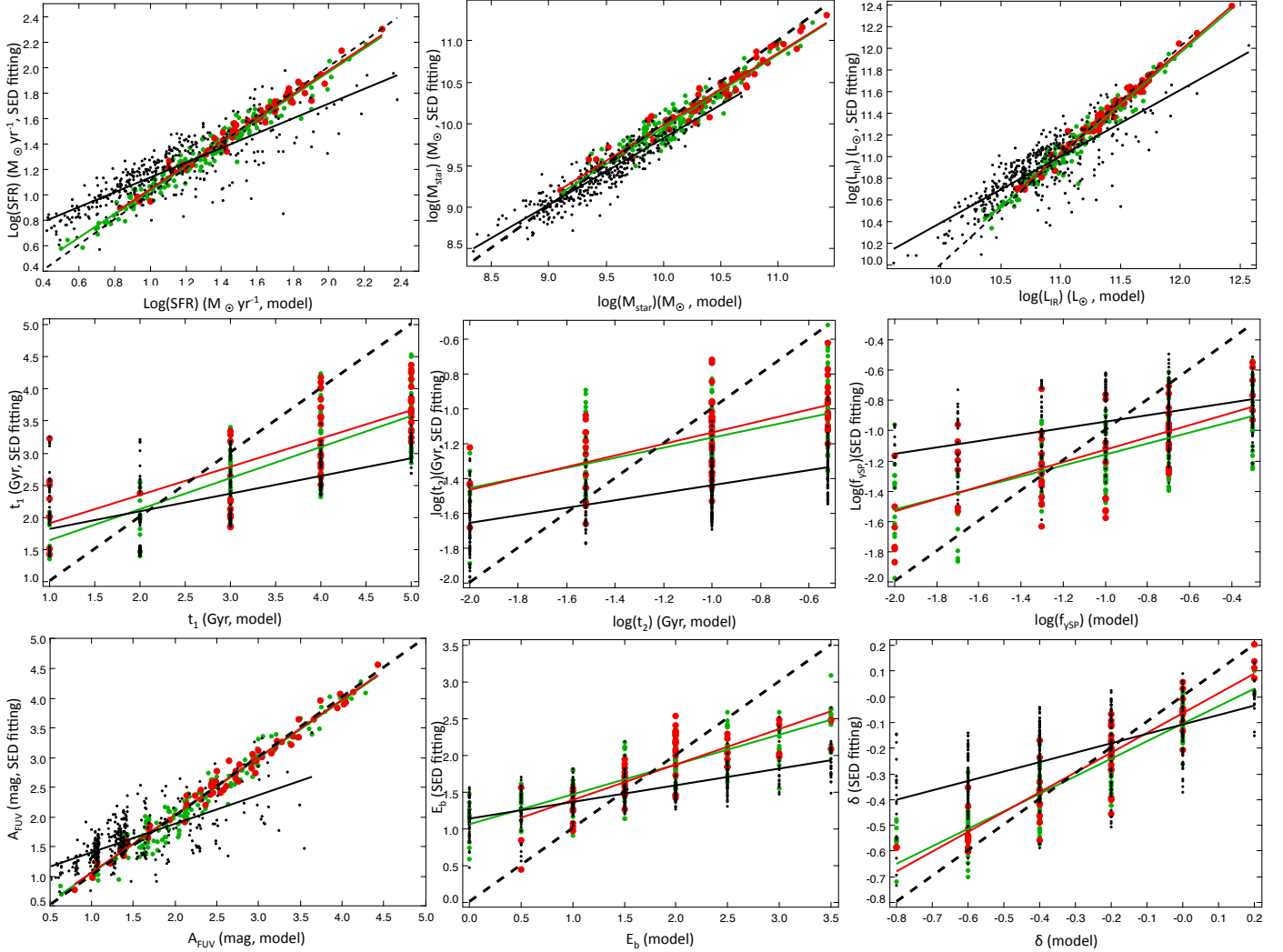
Fig. 3. Comparison of parameters estimated by SED fitting for the catalogue of artificial galaxies. The initial values of the parameters are on the x-axis and the values estimated after SED fitting on the y-axis. The galaxies without IR data are plotted as black dots, the galaxies with only a MIPS detection as green filled circles, and those also detected with PACS as large red filled circles. The regression lines for each subsample are also plotted as solid lines and the 1:1 relation as a dashed line. From the left top to the right bottom, the parameters considered are the SFR, $M_{\rm star}$, $L_{\rm IR}$, t_1, $\log(t_2)$, $\log(f_{\rm ySP})$, $A_{\rm FUV}$, $E_{\rm b}$, and δ.

Table 2. Linear correlation coefficient (R) between the exact value of parameters and the value estimated by the code and its error (standard deviation σ of the PDF) of the estimated values for the sample of artificial galaxies.
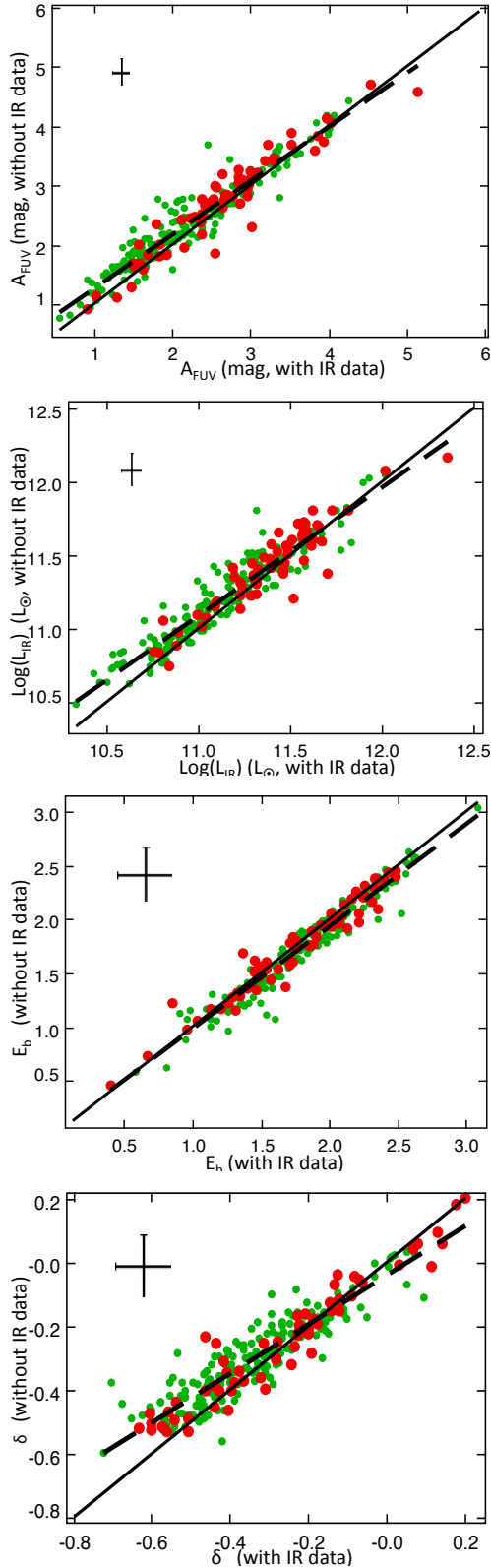
Parameters	No IR data		MIPS data		PACS data	
	R	σ	R	σ	R	σ
$\log(SFR)$ [$M_\odot$ yr^{-1}]	0.86	0.25	0.99	0.11	0.99	0.09
$\log(M_{\rm star})$ [$M_\odot$]	0.92	0.21	0.96	0.15	0.96	0.15
$\log(L_{\rm IR})$ [$L_\odot$]	0.84	0.42	0.98	0.12	0.99	0.08
t_1 [Gyr]	0.67	0.98	0.77	1.02	0.77	1.00
$\log(t_2)$ [Gyr]	0.64	0.41	0.59	0.40	0.67	0.39
$\log(f_{\rm ySP})$	0.53	0.45	0.65	0.44	0.65	0.43
$A_{\rm FUV}$ [mag]	0.75	0.54	0.99	0.28	0.99	0.24
$E_{\rm b}$	0.72	1.00	0.84	0.89	0.82	0.81
δ	0.68	0.24	0.90	0.17	0.93	0.14

the young stars. The average age of the young stellar component is 40 Myr: a steady state in the production of the UV continuum is not reached (Leitherer & Heckman 1995). The distribution of the instantaneous SFR is shown in Fig. 5.
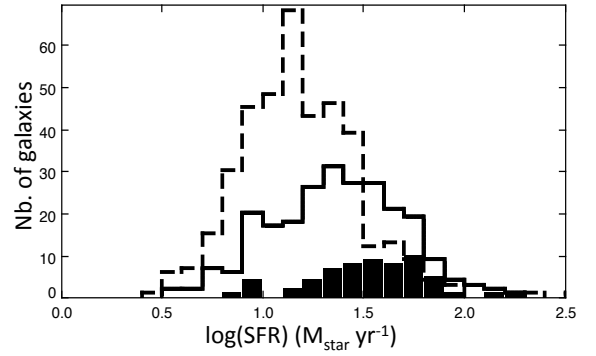
4. The amount of dust attenuation

Several output parameters of the code quantify the amount of dust attenuation. In addition to the V band attenuation of the young stellar population, the total amount of attenuation in the V and FUV bands (for both stellar populations) are also calculated. The distribution of $A_{\rm FUV}$ is shown in Fig. 6. The values range from 0.5 to 5 mag, the largest attenuations being found for galaxies detected with PACS. The mean dust attenuation is equal to 1.6, 2.2, and 2.6 mag for the galaxies without IR data, with MIPS data only, and with MIPS and PACS data, respectively. Note that dust attenuation is likely to be slightly overestimated for galaxies without any IR detection (Sect. 3.2).

The relative amount of attenuation between the young and the old stellar population, expressed in magnitudes, is measured by $f_{\rm att}$. As mentioned above, $f_{\rm att}$ is fixed to 0.5 for our baseline scenario, but we also performed runs with $f_{\rm att}$ as a free parameter allowed to take 3 values: 0.25, 0.5, and 1. This parameter is known to be ill-constrained (Noll et al. 2009b; Buat et al. 2011a). The value 1 is never chosen for the best-fit model and the mean value from the probability distribution function is found to
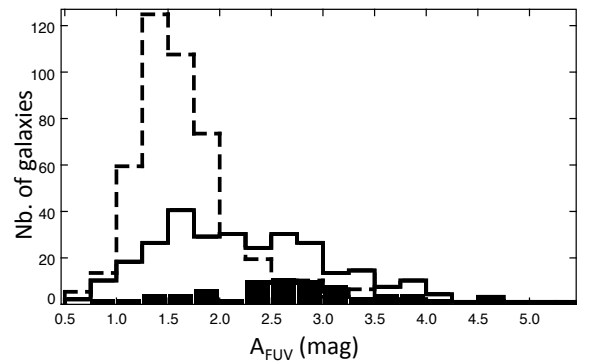
Fig. 5. Histogram of the distribution of the SFR obtained with SED fitting. The distribution with a dashed line corresponds to galaxies without IR detection, the solid line to galaxies detected by MIPS, and the filled histogram is obtained for galaxies detected by PACS.


Fig. 6. Histogram of the dust attenuation in the FUV band. The distribution of A_{FUV} is plotted with a dashed line for galaxies without IR detection, a solid line traces galaxies detected by MIPS, and the filled histogram indicates galaxies detected by PACS.

Fig. 4. Parameters estimated with available IR data (*x*-axis) are compared to those estimated without any IR data. Galaxies with only MIPS data are plotted with small green symbols, galaxies with MIPS and PACS detection with large red symbols. The green dashed line is the result of the linear regression and the black solid line is the 1:1 relation. Typical error bars (1σ) are plotted on the left corner of each plot.

be 0.52 ± 0.06. As a further check, we also ran CIGALE by also fixing f_{att} at 0.25 and 1. All results presented in this work are

found unaffected by the exact value of this parameter. In particular, the distributions of A_{FUV}, L_{IR}, M_{star}, E_b, and δ are not significantly modified when f_{att} is varied.

In Fig. 7, A_{FUV} is plotted versus L_{FUV} and M_{star}. There is a decrease of the upper envelope of the dust attenuation for large L_{FUV} in agreement with other findings based on UV selected samples at similar redshifts (Burgarella et al. 2007; Buat et al. 2009; Burgarella et al. 2011; Heinis et al. 2012). For a given UV luminosity, dust attenuation increases with stellar mass. Average values of A_{FUV} are calculated per bin of UV luminosity and are also reported in Fig. 7: in spite of a large dispersion, the mean value of A_{FUV} is found to decrease when L_{FUV} increases from 2.4 ± 0.8 mag for $\log(L_{FUV}) = 9.7$ [$L_{\odot}$] to 1.5 ± 0.4 mag for $\log(L_{FUV}) = 10.7$ [$L_{\odot}$], which corresponds to a slope -0.9 in Fig. 7. The trend still holds when only galaxies not detected in IR are considered with a less steep decrease (slope reduced to -0.6). The results are not modified if we account for the over-estimation of A_{FUV} for galaxies without an IR detection (cf. Sects. 3.1 and 3.2). So the general variation seen in Fig. 7 cannot be attributed only to the sources detected in IR, with MIPS or PACS. An inverse trend was reported at $z \sim 2$ for Lyman break galaxies by Reddy and collaborators (Reddy et al. 2008, 2010, but see also Burgarella et al. 2011). Interestingly, if we only consider galaxies with $z > 1.8$ to mimic a $z \simeq 2$ selection, our subsample contains galaxies more luminous than $10^{10} L_{\odot}$ and the distribution of A_{FUV} as a function of L_{FUV} is consistent with a flat one (although we do not exclude a slight decrease when L_{FUV} increases). Reddy et al. (2010) also
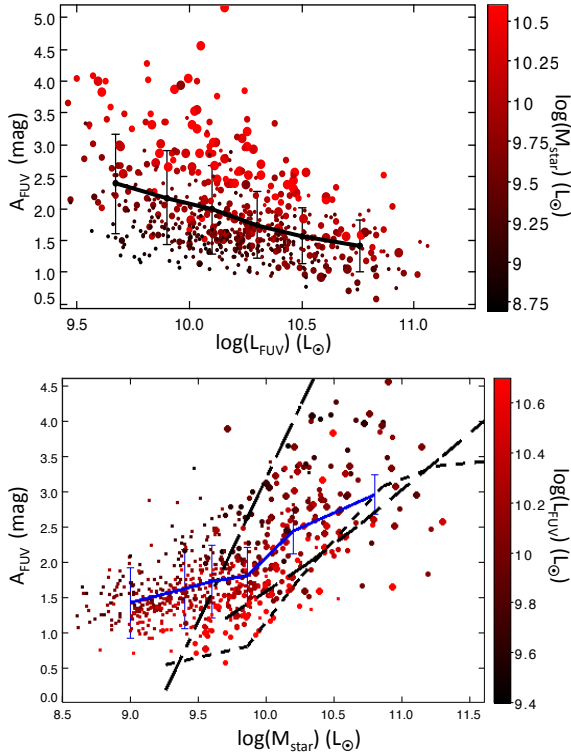
Fig. 7. Dust attenuation in FUV versus observed FUV luminosity and stellar mass. Galaxies with no IR data are plotted as small dots, those with MIPS data with medium dots, and those with MIPS and PACS detection with large dots. *Upper panel:* A_{FUV} versus $\log(L_{FUV})$, colour coded with $\log(M_{star})$. The average values of A_{FUV} per bin of $\log(L_{FUV})$ are overplotted with their standard dispersion, calculated by accounting for the uncertainty on the determination of A_{FUV}. *Lower panel:* A_{FUV} versus $\log(M_{star})$, colour coded with $\log(L_{FUV})$. The average values of A_{FUV} per bin of $\log(M_{star})$ are overplotted with their standard dispersion (blue solid line). Relations from the literature and discussed in the text are overplotted as short dashed line (Martin et al. 2007), dashed line (Buat et al. 2009) at $z \simeq 1$, and dot-dashed line (Pannella et al. 2009) at $z \simeq 2$.

have galaxies with $L_{FUV} > 10^{10} L_{\odot}$, which can explain the apparent discrepancy between their analysis and the present work. The increase of the mean (and dispersion) of dust attenuation for galaxies fainter than $10^{10} L_{\odot}$ in UV is confirmed by Heinis et al. (2012) from a stacking analysis of *Herschel* data in the COSMOS field.

At higher redshift, from studies of the slope of the UV continuum, Bouwens et al. (2009) and Lee et al. (2011) also found a decrease of the dust attenuation with the absolute UV magnitude. However, Finkelstein et al. (2011) and Dunlop et al. (2012) found no significant variation of the UV slope with the absolute UV magnitude.

Dust attenuation is also found to be correlated with the stellar mass as already reported from the local universe up to high redshifts (Martin et al. 2007; Iglesias-Pàramo et al. 2007; Buat et al. 2009; Pannella et al. 2009; Garn & Best 2010; Finkelstein et al. 2011; Sawicki 2012). Martin et al. (2007) and Buat et al. (2009) studied UV selected samples up to $z \sim 1$. They reported variations of A_{FUV} as a function of the stellar mass or K-band rest-frame luminosity. The mean relations they found are shown in Fig. 7 after some transformations. The relation of Martin et al. (2007) for $z = 1$ given in Fig. 7 was obtained for a Salpeter IMF and the models of Bruzual & Charlot (2003). We translate it to a Kroupa IMF by reducing the stellar masses

by 0.24 dex (Arnouts et al. 2007). The contribution of TP-AGB, included in the models of Maraston (2005), is assumed to further reduce the stellar mass by 0.2 dex (Muzzin et al. 2009). Buat et al. (2009) proposed a relation between $\log(L_{IR}/L_{FUV})$, the rest-frame K-band, and the FUV luminosities, and did not find any trend with redshift. The relation reported in Fig. 7 corresponds to a mean FUV luminosity $\langle \log(L_{FUV}) \rangle = 10.2 \, [L_{\odot}]$ representative of our current sample. The K-band luminosity is transformed in stellar mass using the calibration of Arnouts et al. (2007) modified by Ilbert et al. (2010) and A_{FUV} is deduced from $\log(L_{IR}/L_{FUV})$ following Buat et al. (2011a). Although the slope of these correlations are consistent with what we find here, the average dust attenuation at a given stellar mass in these previous works is lower than our present estimate. We also compare our results to the relation obtained by Pannella et al. (2009) at $z = 2$ by comparing SFRs from radio and UV measurements. We apply the corrections described above to translate their results to a Kroupa IMF, also adding the contribution of TP-AGB. Their relation is much steeper than the mean trend we find, leading to larger A_{FUV} at high M_{star}, where IR data are available (i.e. when our estimates are the most reliable). Anyway, it is difficult from this comparison to draw a firm conclusion about the evolution of dust attenuation with redshift at a given stellar mass. Different methods were used to derive stellar masses and dust attenuation factors, and sample selections are also different. A UV selection like that used in this work is biased against high dust attenuation and stellar mass which might induce a shallower relation than for a mass- or SFR-selected sample. Moreover it is very difficult to estimate stellar masses, especially in blue, low-mass galaxies (Ilbert et al. 2010). Stellar masses and dust attenuation must be measured with the same method at all redshifts and within samples selected in the same way in order to be compared. Nevertheless, we can conclude that there is a net increase of dust attenuation at larger stellar masses and that the amount of dust attenuation also varies with the (uncorrected) UV luminosity.
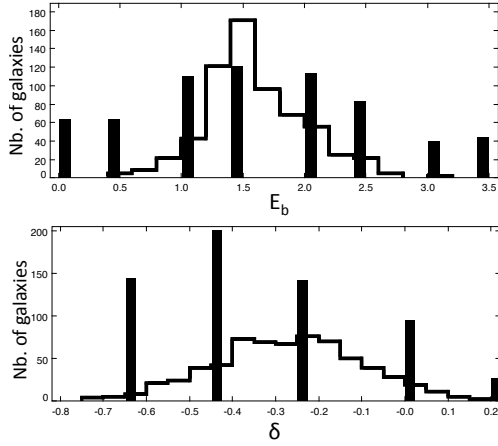
5. The attenuation curve

5.1. Estimation of E_b and δ

The dust attenuation curve is described by the parameters E_b and δ (Eqs. (1) and (2)).

The distributions of these parameters for the best models, estimated as the mean of the PDF, are plotted in Fig. 8. The extreme values of δ are not commonly chosen for the best model obtained by χ^2 minimisation. However, it is not the case for E_b for which the null value is well represented in the best fits. By definition, only positive values of E_b are possible and the output value, given by the code as the mean of the PDF, will be overestimated when the exact value is close to 0. The truncation of the PDF, when its mean value is close to the extreme input values of the parameter distribution, induces an over- or underestimation of the parameter (see Fig. 3 and Sect. 3.2). The amplitude of the effect depends on the exact shape of the PDF. Noll et al. (2009b) discussed the case of a Gaussian distribution with a given standard deviation: for a standard dispersion of 1 unit, typical of our results for E_b (see below and Fig. 10), all the values of E_b lower than 1.2 are affected and the correction ranges from 0.6 for $E_b = 0$ to 0 for $E_b = 1.2$. Another way to quantify the effect, which is less dependent on the shape of the PDF, is to use the correlations obtained for the artificial galaxies between the exact and the measured values of E_b. In Fig. 3, we performed linear regressions, splitting the mock sample in objects without
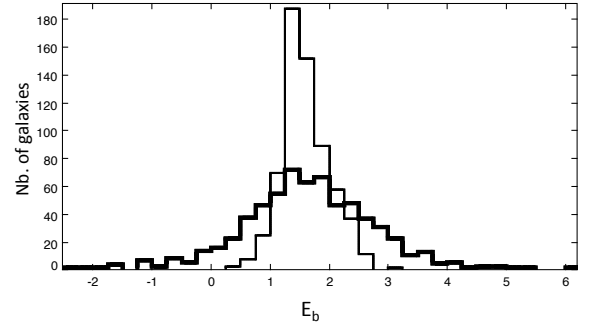
Fig. 8. Distribution of parameters of the attenuation curve. *Upper panel:* distribution of E_b values obtained for the best models (filled histogram) and from the analysis of the PDF (solid line). *Lower panel:* distribution of δ values obtained for the best models (filled histogram) and from the analysis of the PDF (solid line).
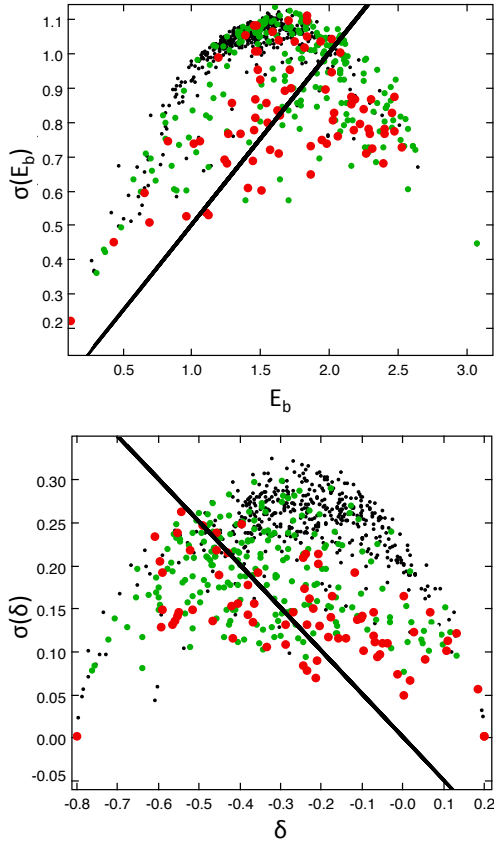

Fig. 9. Distribution of E_b. Thin line: E_b estimated as the mean of the PDF. Thick line: E_b values corrected for edge effects (see text for details). The regressions used for the corrections are: $E_b(\text{SEDfitting}) = 0.26E_b(\text{model}) + 1.08$, $E_b(\text{SEDfitting}) = 0.47E_b(\text{model}) + 0.91$, and $E_b(\text{SEDfitting}) = 0.56E_b(\text{model}) + 0.74$ for the samples without IR detection, with MIPS detections only, and with MIPS and PACS detections, respectvely.

IR detections, those detected by MIPS, and objects detected by PACS. The exact value of E_b ($E_b(\text{model})$) was chosen as independent variable. The resulting regression formulae are applied to the observed sample to correct the values of E_b obtained from the PDF of the SED modelling. The results are plotted in Fig. 9 and the regression formulae are given in the figure caption. As expected, the distribution of the corrected values is found to be broader. Galaxies with unphysically negative values for E_b represent 6% of the sample, whereas all negative values are consistent with a null value of E_b at the one sigma level. The mean value for the entire sample remains unchanged (see below).

To further check the parameter ranges and the reliability of the results, we performed an additional run with a very large range of values for E_b and δ: $-4 < E_b < 4$ and $-0.9 < \delta < 0.9$ with a loose sampling to limit the computation time. Negative values of E_b are found for only 3% of the best models. The fraction reaches 16% for the mean value of the PDF, but except for one object, all these negative mean values are consistent with $E_b = 0$ at a one sigma level. The distribution of δ is very similar to that obtained with the parameters of Table 1. This check confirms the results found with the baseline run and the reliability of the range of values found for E_b and δ.

From an analysis of the mean and standard deviation of each PDF, we can measure the fraction of galaxies for which the bump is securely measured. Mean values and standard deviations for E_b and δ are plotted in Fig. 10. We adopt the same criterion as in Paper I to select sources with a secure detection of the bump as well as those with δ confirmed to be negative, which corresponds to a probability of at least 95% for $E_b > 0$ and $\delta < 0$. Assuming a Gaussian distribution with mean and standard deviation given by the fit, it corresponds to $E_b - 2\sigma_{E_b} > 0$ and $\delta + 2\sigma_\delta < 0$. Using this criterion, 20% of the whole sample is exhibiting a secure bump. The percentage reaches 40% (resp. 47%) for MIPS (resp. PACS) detections. If we apply the corrections for the truncation of the PDF discussed above, the fraction of secure detections of the bump increases to 35% for the whole sample and to 54% (resp. 50%) for MIPS (resp. PACS) detections. A similar percentage (20%) of the whole sample shows a secure negative δ. The percentage is 41% for galaxies detected with MIPS and 43% for those detected by MIPS and PACS. Note that only four SEDs are fitted with a δ value found securely positive (with $\delta - 2\sigma_\delta > 0$). It is worth noting that the error on the

estimation of E_b and δ is lower when the galaxies are detected with MIPS (or PACS).

From the above discussion, it is clear that we must be cautious when reporting mean values for E_b or δ. The mean amplitude of the bump for the whole sample is $\langle E_b \rangle = 1.6 \pm 0.4$. Applying the corrections for the truncation at the edge of the parameter range (see above) only increases the dispersion but not the mean value ($\langle E_b \rangle = 1.6 \pm 1.1$). The mean amplitude is increased to $\langle E_b \rangle = 1.8$ for galaxies detected in IR. These values are larger than those obtained in Paper I. The difference comes from the range of initial values adopted for E_b and the estimation of the parameter as the mean of the PDF. In Paper I, this range was $0 < E_b < 2$, based on the fact that values larger than 2 were never taken for the best models. In the present work, we extend the range of values up to 3.5 (corresponding to the MW value) to minimise the impact of the truncation of the PDF, and because larger values than 2 are also obtained for some of the best models (Fig. 10). While the distribution of values based on χ^2 minimisation are similar (same mean and median: $E_b = 1.5$), the values estimated from the PDF are larger in the present case and were likely to be underestimated in Paper I. We ran the code with the parameters defined in the present work for the sample of galaxies used in Paper I and obtained $\langle E_b \rangle = 1.6 \pm 0.3$.

The mean value $\langle E_b \rangle = 1.6$ corresponds to 45% of the bump amplitude of the MW extinction curve and is similar to that of the LMC supershell region (Fitzpatrick & Massa 2007; Gordon et al. 2003). The large dispersion we find is likely due to the combination of uncertainties in the determination of the bump as well as due to intrinsic differences among galaxies and different environments within a galaxy.

The mean value of δ for the whole sample is $\langle \delta \rangle = -0.27 \pm 0.17$. No significant difference is found when galaxies with and without IR data are considered separately. The value found in Paper I was less negative: running CIGALE on the first sample with the present parameters gives $\langle \delta \rangle = -0.22 \pm 0.18$ compared to $\langle \delta \rangle = -0.13 \pm 0.12$ in Paper I. The difference between both estimates indicates the uncertainty: modifying the range of E_b is likely to imply a difference in the determination of δ. The mean value found here ($\langle \delta \rangle = -0.27$) corresponds to an increase in UV similar to that of the LMC extinction curve (Sect. 6.2). We do not find any trend between E_b and δ (Fig. 11).
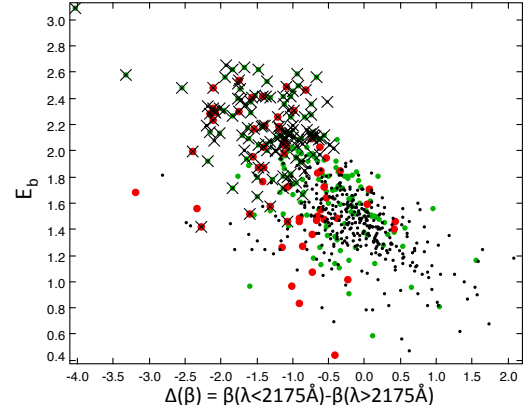
Fig. 12. Amplitude of the bump of the attenuation curve versus the observed variation of the slope of the UV continuum across the bump. The symbols are the same as in Fig. 11.
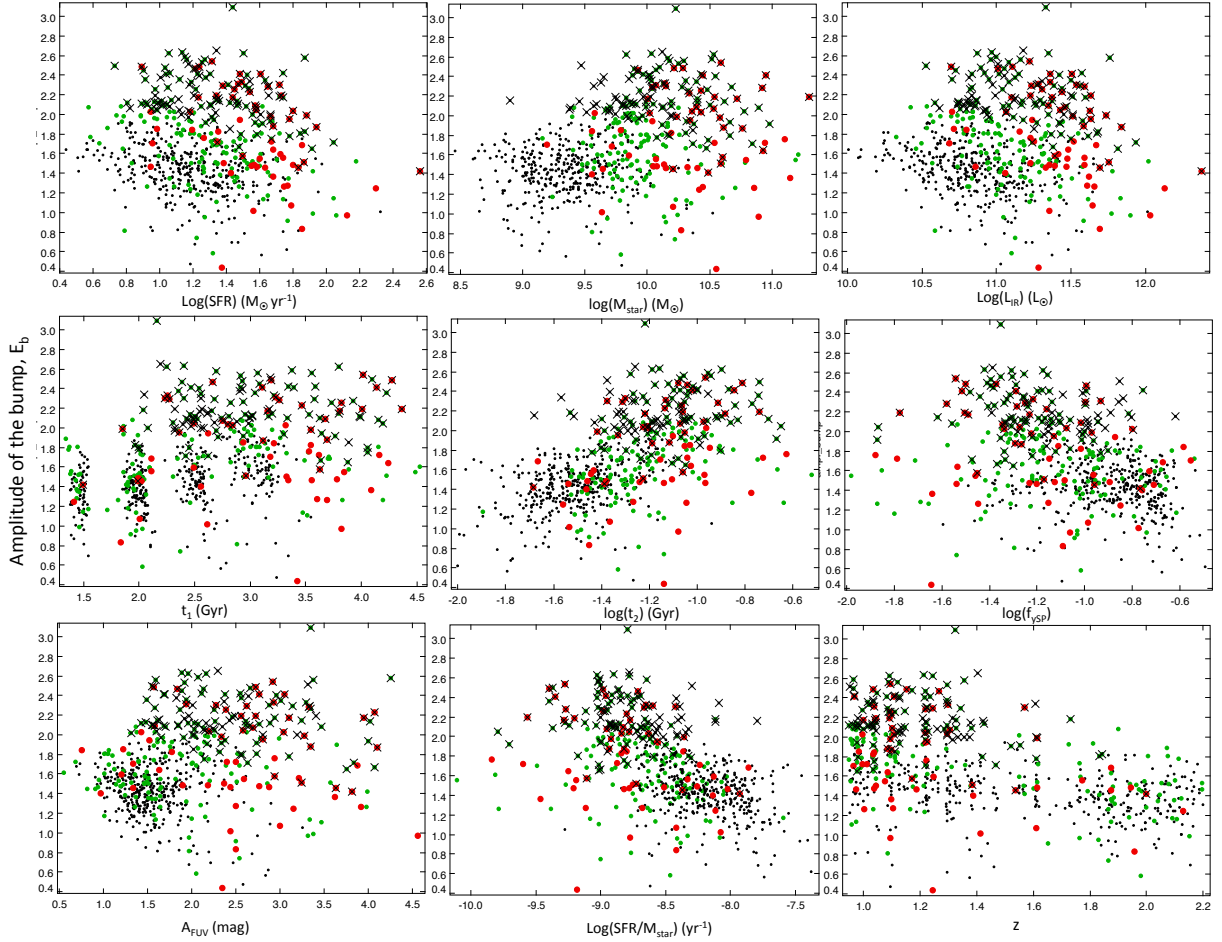
to 1.8 in order to have at least five data points in each subsample. We calculate the values of β corresponding to each wavelength range and subtract the two values with a linear fit: $\Delta\beta = \beta(\lambda < 2175\,\text{Å}) - \beta(\lambda > 2175\,\text{Å})$. The standard error on this differential slope, obtained by adding quadratically the errors on each slope, is of the order of 0.7, i.e. quite large.

A clear trend is found in Fig. 12: all the galaxies with a secure bump detection exhibit a negative value of $\Delta(\beta)$. In order to have reference values, $\Delta(\beta)$ is also calculated on the SEDs of the best models using the same photometric bands as for the real data. Models without bump in the attenuation curve correspond to $\Delta(\beta) \simeq 0.5$. This is consistent with Fig. 12 if we account for the large error found for $\Delta(\beta)$ and the overestimation of E_b for low values of this parameter (Sect. 5.1). Given all these uncertainties, this comparison has to be taken with care. However, our criterion $E_b - 2\sigma_{E_b} > 0$ to select a secure detection of the bump appears to be valid and even conservative, since it corresponds systematically to negative values of $\Delta(\beta)$.

5.3. Discussion

We can summarise the results obtained on the attenuation curve for our galaxy sample: a large range of values is found for the amplitude of the bump and the slope of the curve. Since this dispersion is not significantly reduced by neglecting galaxies with the most uncertain values (see Fig. 10), we can state that these variations probably reflect a real diversity of attenuation curves. These results imply that SED fitting codes must allow for variations of the attenuation curve to fit the UV continuum of galaxies at all redshifts and retrieve reliable attenuations (Ilbert et al. 2009).

The presence of a bump is confirmed in at least 20% of the sources and up to 35% if we account statistically for the truncation of the PDF of this parameter. A steeper attenuation curve than that of Calzetti et al. (2000) is also robustly found in 20% of our galaxies. Noll et al. (2009a) confirm the presence of a bump in ∼30% of their sources, which is consistent with our analysis. The amplitude of the bump is plotted versus the parameters deduced from the SED fitting in Fig. 13. No correlation is found with SFR or $L_{\rm IR}$ and very weak ones may exist with $A_{\rm FUV}$ (correlation coefficient $R = 0.25$) or $M_{\rm star}$ ($R = 0.36$). E_b is found to be lower for younger stellar populations, higher fraction of young stars, high specific SFRs (defined as $SFR/M_{\rm star}$) and higher redshifts. To check the robustness of these trends against SED fitting uncertainties for galaxies not detected in IR,

Fig. 10. Mean (x-axis) and standard deviation (y-axis) for the estimated values of E_b (*upper panel*) and δ (*lower panel*). In the *upper panel*, galaxies with a secure ($>2\sigma$) detection of the bump are located to the right side of the solid line. In the *lower panel*, galaxies with an attenuation curve confirmed to be steeper than the Calzetti one are located to the left side of the solid line (see text for details). The symbols are the same as in Fig. 3.
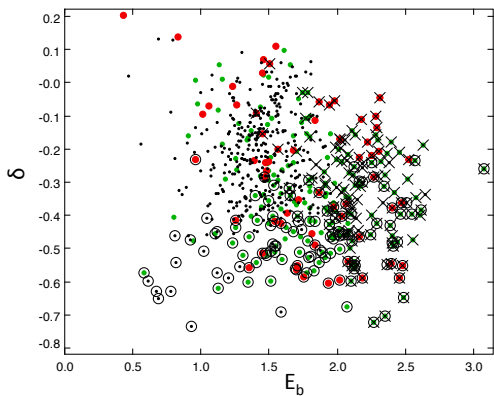
Fig. 11. Slope of the attenuation curve versus amplitude of the bump: symbols are the same as in Fig. 3. Galaxies with a bump detected with a probability higher than 95% are overplotted with crosses and those with secure negative values of δ at the same level of confidence are inscribed in a large circle (see text for details).

5.2. Differential slope and E_b

The imprint of the UV bump in attenuated spectra is expected to lead to a change of the UV slope across the UV bump. Following Noll & Pierini (2005), who defined a spectral index γ_{34}, we split the photometric data in two subsamples corresponding to $\lambda < 2175\,\text{Å}$ and $\lambda > 2175\,\text{Å}$. We restrict the redshift interval from 1.1

Fig. 13. Variation of the bump amplitude E_b. Symbols are the same as in Fig. 3 with crosses overplotted on sources with a secure detection of the bump. From left to right and top to bottom: E_b is plotted versus $\log(SFR)$, $\log(M_{star})$, $\log(L_{IR})$, the age of the old stellar population t_1 (Gyr), the age of the young stellar population $\log(t_2)$ (Gyr), the mass fraction of the young stellar population $\log(f_{ySP})$, A_{FUV} (mag), the specific SFR $\log(SFR/M_{star})$, and the redshift z.

we applied corrections to $\log(SFR)$, $\log(M_{star})$, $\log(L_{IR})$, A_{FUV}, and E_b based on the regression lines plotted in Fig. 3 and found no significant modification (not shown here). Noll et al. (2009a) also found that galaxies with evidence of a 2175 Å feature host older stellar populations than galaxies lacking an evident bump.

The decrease of the bump amplitude in galaxies forming stars actively could be related to a destruction of bump carriers in intense radiation fields or in supernovae shock fronts. Galaxies with high SFRs are recognised to be more compact than galaxies populating the main sequence defined by the SFR-M_{star} relation. The PAH molecules detected in the IR SEDs of the former galaxies exhibit lower equivalent widths (Elbaz et al. 2011) and these molecules are often proposed to be at the origin of the UV bump (Xiang et al. 2011). A deficiency in the production of bump carriers can also be invoked to explain the decrease of E_b in small galaxies, forming stars actively. Most bump carriers or the pre-products of them should be produced by carbon-rich AGB stars, which appear about 300 Myr after the onset of the star formation. Therefore, compact, low mass galaxies with a short but intense star formation history are not good places for the formation of a strong UV bump.

Conversely, radiative transfer models for a clumpy medium, mixing of dust and stars, and dust-clearing effects for older stellar populations predict a decrease in the amplitude of the bump and the effective attenuation even if the extinction law exhibits

a large bump (e.g. Witt & Gordon 2000; Pierini et al. 2004; Panuzzo et al. 2007; Noll et al. 2007). If galaxies with such attenuation properties significantly contribute to the sample, the fraction of galaxies with dust properties that allow for the formation of a strong UV bump should be distinctly higher than observed. Models assuming a clumpy distribution of stars and dust also predict a general flattening of the attenuation curve, although an age-selective attenuation acts in steepening the attenuation curve (Inoue et al. 2006; Panuzzo et al. 2007). A patchy distribution of the dust is needed to obtain an attenuation curve as grey as that of Calzetti et al. (2000) starting with a SMC-like extinction curve (Witt & Gordon 2000; Charlot & Fall 2000). The mean attenuation curve found for our sample galaxies is steeper than the Calzetti et al. (2000) curve: if a significant flattening of the attenuation curve is at work, then the extinction curve must be very steep in our galaxies. The dust grain size distribution plays a major role in the general shape of the extinction curve and a steep increase in UV, which is attributed to a deficit of large grains (e.g. Cartledge et al. 2005), is not unlikely in high-redshift galaxies forming stars very actively.

On the other hand, our sample is characterised by UV bump strengths and attenuation curve slopes close to those typically observed for the extinction curve in the LMC supershell region. Noll et al. (2009a) show that the typical bump widths of luminous star-forming galaxies at these redshifts also agree with the

mean value of the LMC supershell region. Hence, the LMC supershell region may be a model region for high-redshift galaxies with significant UV bumps. In that case, the attenuation curves have to be similar to the extinction curves and this can also be achieved if the dust tends to show a screen-like distribution. This assumption is supported by the observation of strong interstellar absorption lines in galaxies with significant UV bump (Noll & Pierini 2005; Noll et al. 2009a), which can be interpreted by a high covering fraction of young massive stars by dusty gas clouds. Screen-like dust topologies can be produced by large-scale outflows, which is a reasonable assumption for vigorously star-forming high-redshift galaxies.

6. Dust attenuation and UV slope

The slope β of the UV continuum has been widely used to measure dust attenuation in galaxies since the works of Calzetti, Meurer, and collaborators. They showed that the intrinsic value of this slope does not vary a lot as long as a high star formation activity is maintained in galaxies (Leitherer & Heckman 1995; Calzetti 2001): any deviation from this value is assumed to be caused by dust attenuation. This was confirmed by the correlation between the observed slope β and the amount of dust attenuation measured by L_{IR}/L_{FUV} found for local starbursts (e.g. Meurer et al. 1999; Overzier et al. 2011). Although the situation is more complex for non-starbursting galaxies (e.g. Burgarella et al. 2005; Boissier et al. 2007; Hao et al. 2011; Boquien et al. 2012, and references therein), this relation seems to hold for high-redshift systems forming stars intensively, such as Lyman break or BzK galaxies (Daddi et al. 2007; Reddy et al. 2008; Magdis et al. 2010).

We have a reliable measure of β thanks to the intermediate bands included in the analysis. The presence of a bump could modify substantially the value of β measured with broad-band data if they cover the bump area (Burgarella et al. 2005; Buat et al. 2011b). However, our measure of β is insensitive to the presence of the bump (cf. Sect. 2.2). We restrain the following study to galaxies detected in IR. Even if the determination of parameters related to dust attenuation is satisfactory without IR data (Sect. 3), the L_{IR}/L_{FUV}-β diagnostic is very sensitive to variations of the dust attenuation and star formation histories. We prefer to restrict our study to the most secure cases.

6.1. A_{FUV} versus $\log(L_{IR}/L_{FUV})$

We adopt the formalism of Hao et al. (2011) (first proposed by Meurer et al. 1999) to relate A_{FUV} to $\log(L_{IR}/L_{FUV})$ (called IRX hereafter):

$$A_{FUV} = 2.5 \log\left(1 + a_{FUV} \times 10^{IRX}\right), \qquad (3)$$

where $a_{FUV} = 0.595$ for local starbursts (Overzier et al. 2011) and 0.46 for normal star-forming galaxies (Hao et al. 2011). In Fig. 14, the results of our SED fitting are compared to Eq. (3). The local starburst relation is found to be consistent with our data, whereas the relation valid for nearby star-forming galaxies underestimates the dust attenuation in our high-redshift galaxies.

6.2. A_{FUV}-β relation

When the intrinsic UV spectrum is modelled by a power law of exponent β, the relation between the attenuated and unattenuated fluxes, $f(\lambda)$ and $f_0(\lambda)$ (expressed per unit wavelength), and the
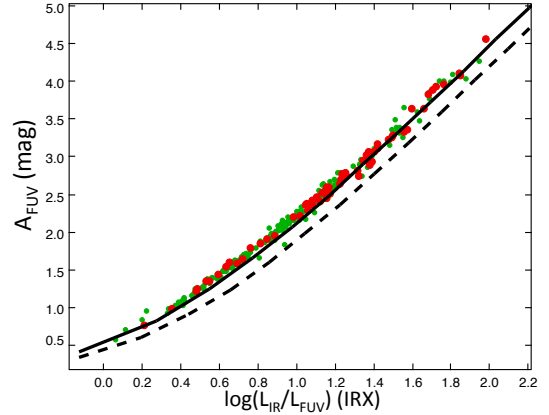
Fig. 14. Dust attenuation in FUV as a function of $\log(L_{IR}/L_{FUV})$ = IRX. The symbols are the same as in Fig. 3. The relation of Overzier et al. (2011) for local starbursts is plotted with a solid line, while the relation proposed by Hao et al. (2011) for local star-forming galaxies is plotted with a black dotted line.

corresponding slopes β and β_0 becomes

$$\beta - \beta_0 = \frac{\log(f(\lambda_1)/f(\lambda_2))}{\log(\lambda_1/\lambda_2)} - \frac{\log(f_0(\lambda_1)/f_0(\lambda_2))}{\log(\lambda_1/\lambda_2)}. \qquad (4)$$

The wavelengths λ_1 and λ_2 are taken in the UV range, where the modelling by a power law is valid. Then, dust attenuation at λ_1 can be written:

$$A(\lambda_1) = \frac{2.5 \log(\lambda_2/\lambda_1)}{1 - A(\lambda_2)/(A(\lambda_1)} \times (\beta - \beta_0) = C(\lambda_1, \lambda_2) \times (\beta - \beta_0), \quad (5)$$

where $A(\lambda_2)/A(\lambda_1)$ depends on the dust attenuation curve (Eq. (1)). In order to be consistent with our SED fitting results, we adopt $\lambda_1 = 1530$ Å (corresponding to the FUV effective wavelength) and $\lambda_2 = 3000$ Å to calculate $C(\lambda_1, \lambda_2)$. Using 1200 and 2500 Å modifies the calculations by less than 1%. We found that $\delta = -0.27 \pm 0.17$ for the entire sample which corresponds to $C(\lambda_1, \lambda_2) = 1.70$ (with a range of $1.46-1.97$ corresponding to the standard deviation for δ). For comparison, $C(\lambda_1, \lambda_2) = 2.3$ for the pure Calzetti law ($\delta = 0$), 1.3 for the SMC and 1.8 for the LMC supershell using the extinction curves of Gordon et al. (2003). We can estimate β_0 from Eq. (5). Using $C(\lambda_1, \lambda_2) = 1.70$, we find $\langle\beta_0\rangle = -2.5 \pm 0.3$, while $\langle\beta_0\rangle = -2.7$ (resp. -2.3) for $C(\lambda_1, \lambda_2) = 1.46$ (resp. 1.97), consistent with the value expected for a young stellar population aged of ~ 40 Myr (see Sect. 3.4). The corresponding relation between β and A_{FUV} ($A_{FUV} = 1.70 \times (\beta + 2.5)$) is plotted in Fig. 15 along with the data. We recall that β is calculated on the entire UV range (Sect. 2). The relation of Overzier et al. (2011) for local starburst galaxies (we consider their inner relation, very close to the original one obtained by Meurer et al. 1999) is also found to reproduce the general observed trend between β and A_{FUV} with a formal scatter for both relations reaching 0.5 dex. Their relation corresponds to $C(\lambda_1, \lambda_2) = 2.05$ and $\beta_0 = -2.19$ with the formalism adopted in this section. Flatter and very dispersed relations are found in the literature (e.g. Buat et al. 2011a; Murphy et al. 2011, and references therein). The relations found by Buat et al. (2011a) and Murphy et al. (2011) for IR-selected galaxies at low and high redshift are reported in Fig. 15. Although a steeper attenuation curve may flatten the relation (cf. Eq. (5)), Buat et al. (2011a) show that a flat distribution with a large dispersion in the A_{FUV}-β diagram is consistent with an attenuation curve only slightly steeper than the Calzetti one and variations in the star formation history with a substantial contribution of old stars.
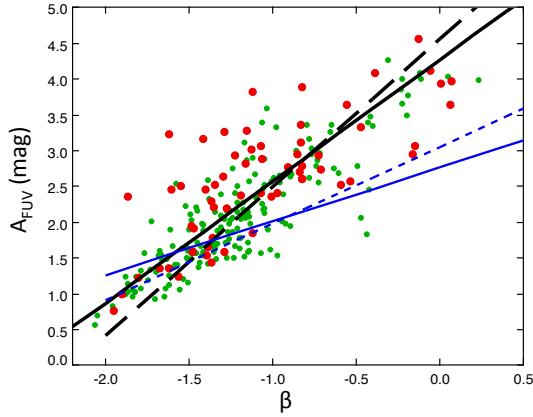
Fig. 15. Dust attenuation as a function of β (same symbols as in Fig. 3). The solid line corresponds to the relation found in this work: $A_{FUV} = 1.70 \times (\beta + 2.5)$. The dashed line corresponds to the relation of Overzier et al. (2011) (their inner relation). The relation found by Murphy et al. (2011) for 24 μm selected galaxies at $0.66 < z < 2.66$ and by Buat et al. (2011a) for nearby galaxies selected at 140 μm are plotted as blue solid and dotted lines, respectively.
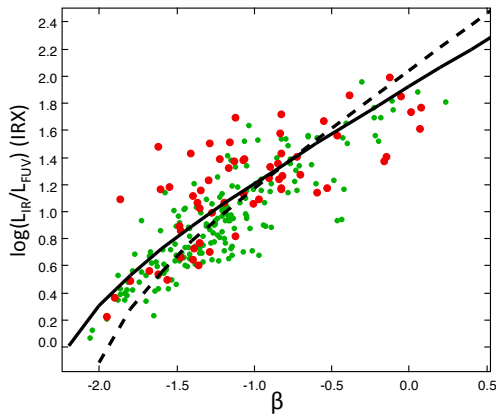
Fig. 16. The observed slope β is plotted versus $\log(L_{IR}/L_{FUV}) = IRX$. The symbols are the same as in Fig. 3. The solid line is the relation found in this work, while the dashed line is that of Overzier et al. (2011).
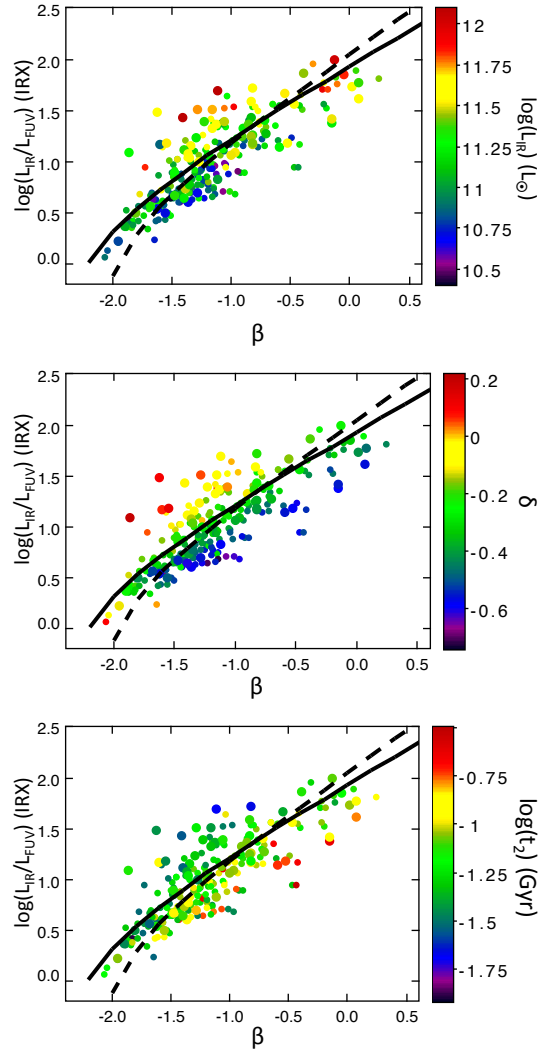

Fig. 17. The observed slope β is plotted versus $\log(L_{IR}/L_{FUV}) = IRX$. The dust luminosity L_{IR} (*top panel*), δ (*median panel*), and the age of the young stellar population t_2 (*bottom panel*) are colour coded. The solid line is the relation found in this work, while the dashed line is that of Overzier et al. (2011).

6.3. IRX-β relation

We combine Eq. (3) for starbursts and Eq. (5) to deduce the IRX-β relation:

$$IRX = \log(10^{0.4 \times 1.7(\beta+2.5)} - 1) - \log(0.595). \qquad (6)$$

The resulting curve is plotted with the data in Fig. 16. The relation proposed by Overzier et al. (2011) for local starbursts is also shown. The modification of the slope of the attenuation curve (steeper than the Calzetti one and similar to that of the LMC supershell) and of the intrinsic UV slope (from ~-2.2 to -2.5) modifies substantially the IRX-β relation. The data are found to roughly follow both laws but a low value of β_0 is necessary to fit the small values of slope and attenuation.

The standard deviation from the Overzier et al. relation reaches 0.27 dex and is reduced to 0.23 dex when the relation derived in this work is used. It is similar to that found by Meurer et al. (1999) for local starburst galaxies. At $z \approx 2$, Reddy et al. (2010) found that typical Lyman break galaxies roughly obey the local starburst IRX-β relation with a formal scatter of 0.38 dex, slightly higher than our value. This relatively low dispersion is probably due to our UV selection and the high star formation

activity of our galaxies, since the original law was first proposed for local UV-selected starburst galaxies. Subpopulations of dusty, IR-luminous galaxies at low and high redshift are known to deviate from the original starburst relation with a higher IRX for a given slope β (Goldader et al. 2002; Chapman et al. 2005; Howell et al. 2010; Papovich et al. 2006). Penner et al. (2012) select dust-obscured galaxies (DOGs) at $z \simeq 2$ and use GOODS-*Herschel* data to study their IR properties. They find that DOGs lie on the left side of the IRX-β relation, with a systematic increase of IRX with β.

The influence of various parameters on the dispersion found in Fig. 16 is explored in Fig. 17. There is a global increase of IRX with L_{IR} for a given value of β. Such a trend was already reported at low and high redshift (e.g. Howell et al. 2010; Chapman et al. 2005, and references therein). We can also investigate the role of the variation of the attenuation curve (δ) and of the star formation history (β_0). As shown in Fig. 17, the sources located above the mean law correspond to δ values less negative than our mean law ($\delta = -0.27$): they are fitted with a greyer attenuation curve. Such a trend with δ is easily explained: for a given slope β these galaxies experience a larger dust attenuation than
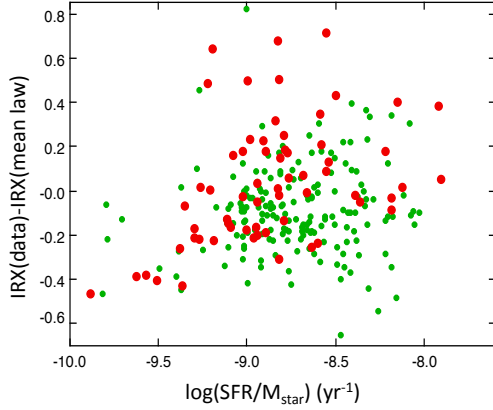
Fig. 18. Distance of the data points in the IRX-β diagram from the mean law found in this work against the specific SFR. Symbols are the same as in Fig. 3.

predicted by our mean law and the fit gives a less efficient reddening and thus a greyer attenuation. β_0 is not an output parameter of CIGALE but its influence can be investigated by using the age of the young stellar populations as a proxy: galaxies with the lowest age (and therefore a small value of β_0) are located well above the mean law and conversely the oldest populations (corresponding to large values of β_0) below it. As a consequence, the intrinsic value of β_0 may also play a role in the locus of the galaxies in the IRX-β diagram (see also Boquien et al. 2012; Heinis et al. 2012).

Elbaz et al. (2011) relate the starburst activity to a higher specific SFR and a high compactness of the star formation. In Fig. 18, the distance to the mean IRX-β law is plotted versus the specific SFR of our galaxies. A weak but positive correlation is found (correlation coefficient $R = 0.20$), which is stronger ($R = 0.51$) when only galaxies detected with PACS are considered. This trend is consistent with a larger contribution of compact regions, which likely have greyer attenuation curves, with increasing specific SFR as proposed by Elbaz et al. (2011).

7. Conclusions

We have studied the dust attenuation properties in a sample of 751 galaxies with $0.95 < z < 2.2$ observed with intermediate-band filters in order to sample correctly the UV rest-frame continuum. IR data from MIPS (290 galaxies) and PACS (76 galaxies) were used when available. Our results are:

1. SED fitting is performed with CIGALE. The dust attenuation law is described with two free parameters: its steepness (δ) and the amplitude of a bump at 2175 Å (E_b). The availability of IR data improves the determination of all the parameters related to dust attenuation. Global parameters such as the SFR, stellar mass, or the amount of dust attenuation are well determined, whereas the detailed star formation history is ill-constrained. Dust attenuations, total IR luminosities, and δ are found to be slightly overestimated in the regime of low attenuation and luminosity when IR data are missing.

2. The dust attenuation in the FUV is found to have a large dispersion for low L_{FUV} ($L_{FUV} < 10^{10} L_\odot$). The mean value of A_{FUV} decreases from 2.4 to 1.5 mag when L_{FUV} increases from $10^{9.7}$ to $10^{10.8} L_\odot$. The dust attenuation is found to increase with stellar mass.

3. The parameters describing the dust attenuation curve, E_b and δ, are found to span a large range of values. This is likely to reflect intrinsic variations of the attenuation curve among galaxies and for different environments within a galaxy. The presence of a bump is confirmed in 20% of the sample, at $z < 1.5$ for 90% of the confirmed detections. A dust attenuation law steeper than that of Calzetti et al. (2000) ($\delta < 0$) is also confirmed for 20% of the sample. These percentages increase to 40% for galaxies with IR detections. The mean values of E_b and δ derived for the whole sample are similar to those found for the extinction curve of the LMC supershell. Finally, E_b is found to be anti-correlated with the specific SFR of galaxies.

4. The relations between A_{FUV} and β (the slope of the UV continuum) and IRX ($\log(L_{IR}/L_{FUV})$) and β are derived for our mean attenuation curve and for galaxies of our sample detected in IR. The intrinsic slope of the UV continuum, β_0, is found equal to -2.5 and the galaxies follow the IRX-β relation with a low dispersion. Galaxies found above the average IRX-β relation have a high IR luminosity and a dust attenuation curve slightly greyer than our mean law, which can be due to a higher compactness of the star formation regions. The age of the young stellar population (i.e. the intrinsic shape of the UV continuum) is likely to also play a role: for a given β, IRX increases when the age of the young stellar population decreases.

References

Arnouts, S., Walcher, C. J., Le Fèvre, O., et al. 2001, A&A, 476, 137
Boissier, S., Gil de Paz, A., Boselli, A., et al. 2007, ApJS, 173, 524
Boquien, M., Buat, V., Boselli, A., et al. 2012, A&A, 539, A145
Bouwens, R. J., Illingworth, G. D., Franx, M., et al. 2009, ApJ, 705, 936
Bruzual, G., & Charlot, S. 2003, MNRAS, 344, 1000
Buat, V., Burgarella, D., Deharveng, J. M., & Kunth, D. 2002, A&A, 393, 33
Buat, V., Takeuchi, T. T., Burgarella, D., Giovannoli, E., & Murata, K. L. 2009, A&A, 507, 693
Buat, V., Giovannoli, E., Takeuchi, T. T., et al. 2011a, A&A, 529, A22
Buat, V., Giovannoli, E., Heinis, S., et al. 2011b, A&A, 533, A93
Burgarella, D., Buat, V., & Iglesias-Páramo, J. 2005, MNRAS, 360, 1413
Burgarella, D., Le Floc'h, E., Takeuchi, T. T., et al. 2007, MNRAS, 380, 986
Burgarella, D., Heinis, S., Magdis, G., et al. 2011, ApJ, 734, L12
Calzetti, D. 2001, PASP, 113, 1449
Calzetti, D., Kinney, A. L., & Storchi-Bergmann, T. 1994, ApJ, 429, 582
Calzetti, D., Armus, L., Bohlin, R. C., et al. 2000, ApJ, 533, 682
Cardamone, C. N., Urry, P. G., Damen, M., et al. 2008, ApJ, 680, 130
Cardamone, C. N., van Dokkum, P. G., Urry, C. M., et al. 2010, ApJS, 189, 270
Charlot, S., & Fall, S. M. 2000, ApJ, 539, 718
Chapman, S., Blain, A. W., Smail, I., & Ivson, R. J. 2005, ApJ, 622, 772
Cartledge, S. I. B., Clayton, G. C., Gordon, K. D., et al. 2005, ApJ, 630, 355
Conroy, C., Schiminovich, D., & Blanton, M. R. 2010, ApJ, 718, 184
da Cunha, E., Charlot, S., & Elbaz, D. 2008, MNRAS, 388, 1595
Daddi, E., Dickinson, M., Chary, R., et al. 2005, ApJ, 631, L13
Daddi, E., Dickinson, M., Morrison, G., et al. 2007, ApJ, 670, 156
Dale, D. A., & Helou, G. 2002, ApJ, 576, 159
Dickinson, M., Giavalisco, M., & the GOODS team 2003, in "The Mass of Galaxies at Low and High Redshift", eds. R. Bender, & A. Renzini (Springer), 324
Dunlop, J. S., McLure, R. J., Robertson, B. E., et al. 2012, MNRAS, 420, 901
Elbaz, D., Daddi, E., Le Borgne, D., et al. 2007, A&A, 468, 33
Elbaz, D., Hwang, H. S., Magnelli, B., et al. 2010, A&A, 518, L29
Elbaz, D., Dickinson, M., Hwang, H. S., et al. 2011, A&A, 533, A119
Finkelstein, F. S., Papovich, C., Salmon, B., et al. 2011, ApJ, 742, 108
Fiore, F., Puccetti, S., Brusa, M., et al. 2009, ApJ, 693, 447
Fitzpatrick, E. L., & Massa, D. 1990, ApJS, 72, 163

Fitzpatrick, E. L., & Massa, D. 2007, ApJ, 663, 320
Garn, T., & Best, P. N. 2010, MNRAS, 409, 421
Giovannoli, E., Buat, V., Noll, S., Burgarella, D., & Magnelli, B. 2011, A&A, 525, A150
Goldader, J. P., Meurer, G., Heckman, T. M., et al. 2002, ApJ, 568, 651
Gordon, K. D., Clayton, G. C., Misselt, K. A., Landolt, A. U., & Wolff, M. J. 2003, ApJ, 594, 279
Hao, C.-N., Kenniccutt, R. C., Jonhson, B. D., et al. 2011, ApJ, 741, 124
Heinis, S., Buat, V., Bethermin, M., et al. 2012, MNRAS, submitted
Hildebrandt, H., Erben, T., Dietrich, J. P., et al. 2006, A&A, 452, 1121
Howell J. H., Armus, L., Mazzarella, J. M., et al. 2010, ApJ, 715, 572
Iglesias-Pàramo, J., Buat, V., Hernandez-Fernandez, J., et al. 2007, ApJ, 670, 279
Ilbert, O., Capak, P., Salvato, M., et al. 2009, ApJ, 690, 1236
Ilbert, O., Salvato, M., Le Floc'h, E., et al. 2010, ApJ, 709, 644
Inoue, A., Buat, V., Burgarella, D., et al. 2006, MNRAS, 370, 380
Kriek, M., van Dokkum, P. G., Whitaker, K. E., et al. 2011, ApJ, 743, 168
Kroupa, P. 2001, MNRAS, 322, 231
Lee, K. S., Dey, A., Reddy, N. A., et al. 2011, ApJ, 733, 99
Leitherer, C., & Heckman, T. M. 1995, ApJS, 96, 9
Leitherer, C., Li, I. H., Calzetti, D., & Heckman, T. M. 2002, ApJS, 140, 303
Magdis, G., Elbaz, D., Daddi, E., et al. 2010, ApJ, 714, 1740
Maraston, C. 2005, MNRAS, 362, 799
Martin, D. C., Small, T., Schiminovich, D., et al. 2007, ApJS, 173, 415
Meurer, G. R., Heckman, T. M., & Calzetti, D. 1999, ApJ, 521, 64
Murphy, E. J., Chary, R. R., Dickinson, M., et al. 2011, ApJ, 732, 126
Muzzin, A., Marchesini, D., van Dokkum, P. G., et al. 2009, ApJ, 701, 1839

Noll, S., & Pierini, D. 2005, A&A, 137, 155
Noll, S., Pierini, D., Pannella, M., & Savaglio, S. 2007, A&A, 472, 455
Noll, S., Pierini, D., Cimatti, A., et al. 2009a, A&A, 499, 69
Noll, S., Burgarella, D., Giovannoli, E., et al. 2009b, A&A, 507, 1793
Overzier, R., Heckman, T. M., Wang, J., et al. 2011, ApJ, 726, L7
Pannella, M., Carilli, C. L., Daddi, E., et al. 2009, ApJ, 698, L116
Panuzzo, P., Granato, G. L., Buat, V., et al. 2007, MNRAS, 375, 640
Papovich, C., Moustakas, L. A., Dickinson, M., et al. 2006, ApJ, 640, 92
Penner, K., Dickinson, M., & Pope, A. 2012, ApJ, submitted
Pierini, D., Gordon, K. D., Witt, A. N., & Madsen, G. J. 2004, ApJ, 617, 1022
Pilbratt, G., Riedinger, J. R., Passvogel, T., et al. 2010, A&A, 518, L1
Poglitsch, A., Waelkens, C., Geis, N., et al. 2010, A&A, 518, L2
Reddy, N. A., Steidel, C. C., Pettini, M., et al. 2008, ApJ, 692, 778
Reddy, N. A., Erb, D. K., Pettini, M., Steidel, C. C., & Shapley, A. E. 2010, ApJ, 712, 1070
Reddy, N., Dickinson, M., Elbaz, D., et al. 2012, ApJ, 744, 154
Rigopoulou, D., Magdis, G., Ivison, R., et al. 2010, MNRAS, 409, L7
Sawicki, M. 2012, MNRAS, 421, 2187
Siebenmorgen, R., Freudling, W., Krügel, E., & Haas, M. 2004, A&A, 421, 129
Tuffs, R., Popescu, C., Volk, H. J., Kylafis, N. D., & Dopita, M. A. 2004, A&A, 419, 821
Wijesinghe, D. B., Hopkins, A. M., Sharp, R., et al. 2011, MNRAS, 410, 2291
Wild, V., Charlot, S., Brinchmann, J., et al. 2011, MNRAS, 417, 1760
Witt, A. N., & Gordon, K. D. 2000, ApJ, 528, 799
Wuyts, S., Labbé, I., Forster-Schreiber, N. M., et al. 2008, ApJ, 682, 985
Wuyts, S., Forster-Schreiber, N., Lutz, D., et al. 2011, ApJ, 738, 106
Xiang, F. Y., Li, A., & Zhong, J. X. 2011, ApJ, 733, 91